Progress In Electromagnetics Research B, Vol. 39, 225–239, 2012

FOUR-DIMENSIONAL SAR IMAGING SCHEME BASED ON COMPRESSIVE SENSING

X. Z. Ren[1,*], Y. F. Li[1], and R. L. Yang[2]

[1]College of Information Science and Engineering, Henan University of Technology, Zhengzhou, China

[2]The Institute of Electronics, Chinese Academy of Sciences, Beijing, China

Abstract—The observation data obtained from 4-D synthetic aperture radar system is sparse and non-uniform in the baseline-time plane. Hence, the imaging results acquired by traditional Fourier-based methods are limited by high sidelobes. Considering the sparse structure of actual target space in high frequency radar application, a novel 4-D imaging scheme based on compressive sensing is proposed in this paper. Firstly, the azimuth-slant range image is acquired by traditional pulse compression. Then, the basis matrix and the measurement matrix are constructed based on the sparse distribution of the radar positions and the signal form after the azimuth-slant range compression. Moreover, a weighted matrix related to the supporting field of the target is introduced to the cost function. Finally, the elevation-velocity image is reconstructed with this new cost function. Simulation results confirm the effectiveness of the proposed method.

1. INTRODUCTION

Traditional synthetic aperture radar (SAR) systems can reconstruct 2-D images of the investigated area with all-weather capability [1–4], and SAR tomography extends the synthetic aperture principle of SAR into the height direction for 3-D imaging. Tomography SAR adds multiple baselines in the direction perpendicular to the azimuth and to the line of sight and forms an additional synthetic aperture in the height direction. Therefore it has a resolving capability along this dimension [5, 6]. In particular, it can be an interesting

Received 12 December 2011, Accepted 8 March 2012, Scheduled 15 March 2012

* Corresponding author: Xiao-Zhen Ren (rxz235@163.com).

tool for applications involving estimation of forest height, ground topography, and for solving layover effect in natural or urban areas. However, the displacements velocity of scatterers can not be measured in tomography SAR.

Differential synthetic aperture radar interferometry (D-InSAR) is an advanced operation mode of SAR interferometry (InSAR) that allows one to investigate Earth surface deformation phenomena by exploiting the phase difference of SAR image pairs relevant to temporally separated observations of the investigated area [7, 8]. D-InSAR is fruitfully applied for detecting and mapping deformations (with centimeter to millimeter accuracy) of the ground and monitoring buildings, glacier flows, and slope instabilities. However, this technique assumes that there is only a single dominant scatterer within one resolution cell. That is to say, with D-InSAR it is possible to provide an average measurement of the ground deformation, but the distribution of scatterers in height is underdetermined

4-D SAR imaging, also referred to as differential SAR tomography, has been recently proposed as a natural extension of SAR tomography [9]. It exploits both the multibaseline and multitemporal nature of multipass data to allow distinguishing multiple scatterers at different heights and deformation velocities within the same azimuth-range resolution cell. Therefore, it allows measuring the scattering distribution in the azimuth-range-height-velocity 4-D space. In practice, 4-D imaging technique has been investigated in other fields by solving a nonlinear inverse problem, such as electrical capacitance, electrical impedance and magnetic induction tomography imaging [10–13]. Unfortunately, for the current 4-D SAR system, the obtained observation data is sparse and non-uniform in the baseline-time plane. Hence, the imaging results obtained by traditional methods are limited by high sidelobes.

To overcome these difficulties, an adaptive estimation algorithm based on Capon filtering was proposed to achieve sidelobe reduction [9]. However, it requires the use of multilook data to estimate the data covariance matrix. Subsequently, also singular value decomposition (SVD) and inverse problem based methods were considered to focus the height-velocity image [14–16]. An additional problem is that these methods should handle an ill-conditioning inverse problem.

In a recent work, a new sampling theory referred as compressive sensing (CS) has been proposed for SAR applications [17–20]. CS is a model-based framework for data acquisition and signal recovery based on the premise that a signal having a sparse representation in one basis can be reconstructed from a small number of measurements collected in a second basis that is incoherent with the first. Because

the targets can be modeled as sparse based on the hypothesis of multi-center of scattering in high frequency radar application [21], the 4-D SAR imaging can be transformed into the problem of sparse signal representation, and CS-based method can be used for image reconstruction.

The main topic of this paper is to present a novel 4-D SAR imaging scheme based on CS. The rest of the paper is organized as follows. Section 2 presents the geometric and signal model of 4-D SAR system. In Section 3, a new 4-D SAR imaging scheme based on CS is described in detail. The performance of the method is investigated by simulated data in Section 4. Finally, Section 5 gives a brief conclusion.

2. 4-D SAR IMAGING PRINCIPLE

The system geometry of 4-D SAR is shown in Figure 1. x, y, and r denote the range, azimuth, and slant range directions, respectively. The direction perpendicular to the azimuth and to the slant range is defined as the height direction, which is marked as s. Generally, we consider M passes over the interested area at a fixed time, and the M passes are supposed to be parallel to the azimuth direction. Then, one 2-D SAR image can be derived by one pass, and M SAR images are derived by M passes at the same time. After repeating the above experiment at N different times t_n $(n = 1, 2, \ldots, N)$, the MN SAR images can be derived. Suppose that all SAR images have been coregistered first, and then, the azimuth and slant range positions of each scatterer in all SAR images are the same. That is to say, we have MN data samples corresponding to each azimuth-slant range cell, which are given by $h_{m,n}$ $(m = 1, 2, \ldots, M;\ n = 1, 2, \ldots, N)$, where

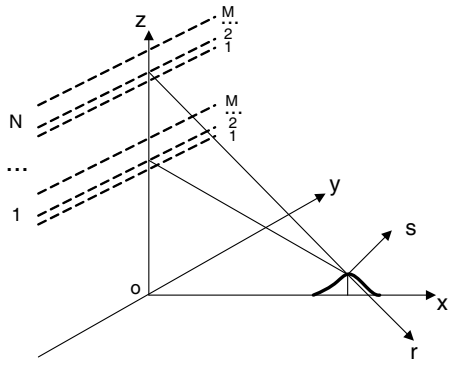

Figure 1. The system geometry of 4-D SAR.

$h_{m,n}$ denotes the data received by the mth pass at the time t_n. For a scatterer positioned at (y', r'), distributed along the height direction and that move with mean velocity v, the obtained 2-D SAR image can be written as [22]

$$h_{m,n}=\iint dydrf(y'-y,r'-r)\iint dsdv\gamma(y,r,s,v)\exp\left[-j\frac{4\pi}{\lambda}R_{m,n}(r,s,v)\right] \tag{1}$$

where $f(y', r')$ is the azimuth-slant range 2-D point spread function, $\gamma(y, r, s, v)$ is the reflectivity function, and $R_{m,n}(r, s, v)$ represents the distance between the sensor related to the mth acquisition at the time t_n and the scatterer point

$$\begin{aligned} R_{m,n}(r,s,v) &= \sqrt{(r-b_{//(m,n)})^2+(s-b_{\perp(m,n)})^2}+vt_n \\ &\approx r-b_{//(m,n)}+\frac{(s-b_{\perp(m,n)})^2}{2(r-b_{//(m,n)})}+vt_n \end{aligned} \tag{2}$$

where $b_{//(m,n)}$ is the baseline parallel to the line of sight, and $b_{\perp(m,n)}$ is the baseline orthogonal to the line of sight. t_n is the acquisition time, supposed that $t_1 = 0$.

Equation (1) represents that the azimuth-slant range focused image of 4-D SAR can be obtained with the same imaging process of classical 2-D imaging SAR. The information of the height and the deformation velocity are included in the phase factor in (1). For sake of simplicity, we assume the azimuth-slant range 2-D point spread function $f(y', r')$ to approximate an ideal 2-D Dirac function. Consequently, the imaging process of the height-velocity can be separated from the azimuth and slant range directions in 4-D SAR. Therefore, the 4-D imaging process can be divided into two steps. The azimuth-slant range focused image can be obtained first, and then, the height-velocity focusing is performed. As the first step is a general 2-D imaging process, this paper focuses on the second step.

Submitting $f(y', r') = \delta(y')\delta(r')$ into (1) yields

$$h_{m,n}=\int_{-v_o}^{v_o}\int_{-s_o}^{s_o}\gamma(s,v)\exp\left[-j\frac{4\pi}{\lambda}R_{m,n}(s,v)\right]dsdv \tag{3}$$

where $2s_o$ is the extent in the height direction, and $2v_o$ is the extent in the velocity direction. The phase factor in (3) comprises a quadratic distortion, which can be compensated by deramping procedure

$$y_{m,n}=h_{m,n}\exp\left[j\frac{4\pi}{\lambda}R_{m,n}(0,0)\right]=\int_{-v_o}^{v_o}\int_{-s_o}^{s_o}\gamma(s,v)g_{m,n}(s,v)dsdv \tag{4}$$

where

$$g_{m,n}(s,v) = \exp\left[j2\pi\left(\frac{2s}{\lambda r}b_{\perp(m,n)} + \frac{2v}{\lambda}t_n\right)\right], \quad m = 1,2,\ldots,M; \quad n = 1,2,\ldots,N \tag{5}$$

Equation (4) shows that the $M \times N$ received data $\mathbf{Y}$ are samples of the 2-D Fourier transform of the scattering distribution in the height-velocity plane. For many regularly spaced baselines and acquisition times, 2-D Fourier analysis can provide satisfactory imaging results. However, in practice, only one or a few baselines per each pass can be considered, this would realize a sparse bidimensional sampling of the 2-D baseline-time plane. Therefore, new imaging scheme should be considered to obtain satisfactory reconstruction.

3. 4-D SAR IMAGING SCHEME BASED ON COMPRESSIVE SENSING

Compressive sensing is a new sampling theorem [23–25]. Consider a discrete signal x with a length of L, known to have sparse representation in an orthogonal basis $\mathbf{\Psi}$, and then the signal x can be represented as

$$x = \mathbf{\Psi}\boldsymbol{\gamma} \tag{6}$$

where $\boldsymbol{\gamma}$ is the projection coefficient vector. If $\boldsymbol{\gamma}$ has only J nonzero or significant elements, signal x is denoted as J-sparse in orthogonal basis $\mathbf{\Psi}$.

Within the CS framework, the signal x can be reconstructed from K $(K = O(J \cdot \log(L/J)))$ measurements y only if the measurements were obtained in a sensing basis $\mathbf{\Phi}$, which is mutually incoherent to the basis $\mathbf{\Psi}$. Therefore, the measurement vector can be written as

$$\mathbf{y} = \mathbf{\Phi}x = \mathbf{\Phi\Psi}\boldsymbol{\gamma} \tag{7}$$

When the mapping matrix $\mathbf{\Phi\Psi}$ follows the restricted isometry property (RIP), $\boldsymbol{\gamma}$ can be recovered exactly from K measurements $\mathbf{y}$ by solving an l norm minimization problem

$$\hat{\boldsymbol{\gamma}} = \min \|\boldsymbol{\gamma}\|_0 \text{ s.t. } \mathbf{y} = \mathbf{\Phi\Psi}\boldsymbol{\gamma} \tag{8}$$

The imaging process of 4-D SAR is to reconstruct the reflectivity function. As described in section 2, the 4-D SAR imaging can be focused on the height-velocity imaging. That is to find proper reflectivity function $\gamma\ (s,\ v)$ meeting the integral

$$y_{m,n} = \int_{-v_o}^{v_o}\int_{-s_o}^{s_o} \gamma(s,v)g_{m,n}(s,v)dsdv \tag{9}$$

For numerical analysis, the continuous-space system model of (9) can be approximated by discrete system model

$$y_{K\times 1}=\begin{bmatrix} y(1)\\ y(2)\\ \vdots\\ y(K)\end{bmatrix}=\begin{bmatrix} g_1(1) & g_1(2) & g_1(3) & \dots & g_1(L)\\ g_2(1) & g_2(2) & g_2(3) & \dots & g_2(L)\\ \vdots & \vdots & \vdots & \vdots & \vdots\\ g_K(1) & g_K(2) & g_K(3) & \dots & g_K(L)\end{bmatrix}$$
$$\begin{bmatrix} \gamma(1)\\ \gamma(2)\\ \gamma(3)\\ \vdots\\ \gamma(L)\end{bmatrix}=G_{K\times L}\gamma_{L\times 1} \tag{10}$$

where

$$\mathbf{y}_{K\times 1}=\begin{bmatrix} y(1)\\ y(2)\\ \vdots\\ y(K)\end{bmatrix}=\mathrm{vec}\begin{bmatrix} y_{1,1} & y_{1,2} & \cdots & y_{1,N}\\ y_{2,1} & y_{2,2} & \cdots & y_{2,N}\\ \vdots & \vdots & \vdots & \vdots\\ y_{M,1} & y_{M,2} & \cdots & y_{M,N}\end{bmatrix} \tag{11}$$

and

$$\boldsymbol{\gamma}_{L\times 1}=\begin{bmatrix} \gamma(1)\\ \gamma(2)\\ \vdots\\ \gamma(L)\end{bmatrix}$$
$$=\mathrm{vec}\begin{bmatrix} \gamma(\Delta_s,\Delta_v) & \gamma(\Delta_s,2\Delta_v) & \dots & \gamma(\Delta_s,Q\Delta_v)\\ \gamma(2\Delta_s,\Delta_v) & \gamma(2\Delta_s,2\Delta_v) & \dots & \gamma(2\Delta_s,Q\Delta_v)\\ \vdots & \vdots & \vdots & \vdots\\ \gamma(P\Delta_s,\Delta_v) & \gamma(P\Delta_s,2\Delta_v) & \dots & \gamma(P\Delta_s,Q\Delta_v)\end{bmatrix} \tag{12}$$

where $\mathrm{vec}(\cdot)$ is the vec-operator which stacks the columns of the matrix between parenthesis. $K=M\times N$, $L=P\times Q$. $y_{m,n}$ $(m=1,2,\dots M;\ n=1,2,\dots,N)$ are the $M\times N$ received data obtained by (4). γ $(p\Delta_s,q\Delta_v)$ $(p=1,2,\dots P;\ q=1,2,\dots,Q)$ are the discrete samplings of the reflectivity function $\gamma(s,v)$, $p\Delta_s\,(p=1,2,\dots P)$ denote the discrete height sampling positions, and $q\Delta_v\,(q=1,2,\dots,Q)$ denote the discrete velocity sampling points. Moreover, the element $g_k(l)$in the matrix $G_{K\times L}$ is defined by

$$g_k(l)=g_{(n-1)M+m}((q-1)P+p)=\exp\left[j2\pi\left(\frac{2p\Delta_s}{\lambda r}b_{\perp(m,n)}+\frac{2q\Delta_v}{\lambda}t_n\right)\right] \tag{13}$$

where $k = 1, 2, \ldots, K;\ l = 1, 2, \ldots, L$. The values of k and l are defined by $k = (n-1)M + m$ $(m = 1, 2, \ldots, M;\ n = 1, 2, \ldots, N)$ and $l = (q-1)P + p$, $(p = 1, 2, \ldots P;\ q = 1, 2, \ldots, Q)$, respectively.

In conclusion, the objective of 4-D SAR imaging is to retrieve the reflectivity coefficient $\boldsymbol{\gamma}_{L\times 1}$. Because the scene of interest can be modeled by a set of point scatterers reflecting impinging electromagnetic waves isotropically to all receivers in high frequency radar application, the reflectivity coefficient $\boldsymbol{\gamma}_{L\times 1}$ to be reconstructed is sparse in the object domain, which is spanned by the orthogonal basis $\boldsymbol{\Psi} = \mathbf{I}_{L\times L}$.

According to (10), the sensing basis $\boldsymbol{\Phi}$ can be selected as

$$\boldsymbol{\Phi} = G_{K\times L} \tag{14}$$

In order to expect a valid solution to the highly undetermined system in (10), the mapping matrix $\boldsymbol{\Theta} = \boldsymbol{\Phi}\boldsymbol{\Psi}$ must follow the restricted isometry property (RIP) according to the theory of CS [24]. A matrix $\boldsymbol{\Theta}$ is said to satisfy the RIP of order J with constants $\delta_J \in (0, 1)$ if

$$(1 - \delta_J) \|v\|_2^2 \leq \|\Theta v\|_2^2 \leq (1 + \delta_J) \|v\|_2^2 \tag{15}$$

for any v such that $\|v\|_0 \leq J$. The RIP essentially states that all subsets of J columns taken from $\boldsymbol{\Theta}$ are in fact nearly orthogonal. Direct design of $\boldsymbol{\Theta}$ based on this property is challenging, as it is combinatorial in nature. In fact, one can show that the RIP can be achieved with high probability by simply assumes that the projections $\boldsymbol{\Phi}$ are drawn at random [23].

Even though the RIP can be established for some matrices, in practice there is no computationally feasible way to check this property. An alternative approach is to ensure the sensing matrix $\boldsymbol{\Phi}$ mutually incoherent with the basis $\boldsymbol{\Psi}$. The mutual coherency is defined as:

$$\mu(\boldsymbol{\Phi}, \boldsymbol{\Psi}) = \max_{i,j} \frac{|\langle \phi_i, \psi_j \rangle|}{\|\phi_i\|_2 \|\psi_j\|_2} \tag{16}$$

where the ϕ_i are rows from $\boldsymbol{\Phi}$, and ψ_j are columns from $\boldsymbol{\Psi}$. The $\boldsymbol{\Phi}$ and $\boldsymbol{\Psi}$ are mutually incoherent if $\mu(\boldsymbol{\Phi}, \boldsymbol{\Psi})$ is small. It has been shown that the mutual coherence satisfies the following bound [25]

$$\frac{1}{\sqrt{L}} \leq \mu(\boldsymbol{\Phi}, \boldsymbol{\Psi}) \leq 1 \tag{17}$$

When $\mu(\boldsymbol{\Phi}, \boldsymbol{\Psi})$ is close to its minimum value of $1/\sqrt{L}$, the bases $\boldsymbol{\Phi}$ and $\boldsymbol{\Psi}$ are completely different. When $\mu(\boldsymbol{\Phi}, \boldsymbol{\Psi})$ approaches its maximum value of 1 then $\boldsymbol{\Phi}$ and $\boldsymbol{\Psi}$ are very similar. In our case of 4-D SAR imaging, the sensing matrix $\boldsymbol{\Phi} = \mathbf{G}_{K\times L}$ is determined by (13), which is a partial Fourier matrix where K rows of the Fourier

matrix are selected at random, $\mathbf{\Psi} = \mathbf{I}_{L\times L}$ is the identity matrix, then the coherence $\mu(\mathbf{\Phi}, \mathbf{\Psi})$ between $\mathbf{\Phi}$ and $\mathbf{\Psi}$ attains its minimum value $1\Big/\sqrt{L}$. That is to say, the $\mathbf{\Phi}$ and $\mathbf{\Psi}$ have the maximal incoherence in the 4-D SAR imaging system, and the sparse signal $\boldsymbol{\gamma}_{L\times 1}$ will be recovered exactly with high probability.

Within the CS framework, the sparse signal $\boldsymbol{\gamma}_{L\times 1}$ can be reconstructed by l norm minimization

$$\hat{\boldsymbol{\gamma}} = \min \|\boldsymbol{\gamma}\|_0 \text{ s.t. } y = \mathbf{\Phi}\mathbf{\Psi}\boldsymbol{\gamma} \tag{18}$$

In the more realistic case some noise is added on the measurements

$$y = \mathbf{\Phi}\mathbf{\Psi}\boldsymbol{\gamma} + \mathbf{n} \tag{19}$$

with $\mathbf{n}$ a complex Gaussian vector with zero mean and power σ^2. Therefore, the solution of (18) can be replaced by constraining the l_2 norm of the error in measurements to be less than some threshold ε

$$\hat{\boldsymbol{\gamma}} = \min \|\boldsymbol{\gamma}\|_0 \text{ s.t. } \|\mathbf{\Phi}\mathbf{\Psi}\boldsymbol{\gamma} - \mathbf{y}\|_2 \le \varepsilon \tag{20}$$

where ε is a small positive number.

The l_0 norm can obtain the optimally sparse solution of a signal. Unfortunately, the l_0 norm is computationally difficult to solve, as it involves NP-hard enumerative search. A common alternative is to consider the convex problem using an l_1 norm as a proxy for the l_0 norm. For $K = O(J \cdot \log(L/J))$, it can be shown that l_1 norm minimization leads to the same result as l norm minimization [24]

$$\hat{\boldsymbol{\gamma}} = \min \|\boldsymbol{\gamma}\|_1 \text{ s.t. } \|\mathbf{\Phi}\mathbf{\Psi}\boldsymbol{\gamma} - \mathbf{y}\|_2 \le \varepsilon \tag{21}$$

However, in practice there is still error using an l_1 norm instead of the l_0 norm in the low signal-to-noise ratio (SNR) condition. Since the larger and smaller coefficients have the different contributions to the object function in the l_1 norm minimization, the larger coefficients are penalized more heavily in the l_1 norm than smaller coefficients, unlike the more democratic penalization of the l_0 norm, which may reduce the contribution of the larger coefficients, and can not give strict constraint on the smaller coefficients. To address this imbalance, a weighted formulation of l_1 norm minimization designed to more democratically penalize nonzero coefficients is proposed in [26]

$$\hat{\boldsymbol{\gamma}} = \min \|\mathbf{W}\boldsymbol{\gamma}\|_1 \quad \text{s.t.} \quad \|\mathbf{\Phi}\mathbf{\Psi}\boldsymbol{\gamma} - \mathbf{y}\|_2 \le \varepsilon \tag{22}$$

where $\mathbf{W}$ is a diagonal matrix with $w_1, w_2, \ldots, w_L$ on the diagonal and zeros elsewhere, and $w_1, w_2, \ldots, w_L$ are positive weights. In [26], Candes et al. have proven that the weights should relate inversely to the true signal magnitude

$$w_i = \frac{1}{\gamma_i + \delta}, \quad i = 1, 2, \ldots L \tag{23}$$

where δ is a small positive number.

The main idea of this weighted step is to construct the appropriate weights in the optimization problem and reduce the influence of noise. Therefore, the weights should be selected to find the correct signal components and counteract the influence of the noise. According to (22) and (23), it is obvious that the large entries in w_i force the solution of $\boldsymbol{\gamma}$ to concentrate on the indices where w_i is small, and correspond precisely to the indices where $\boldsymbol{\gamma}$ is nonzero.

Compared with the l_1 norm model, it is easier to obtain the optimally sparse solution of the signal for the weighted l_1 norm minimization. Therefore, a weight matrix is introduced to the 4-D SAR imaging process. From (23) we can get that the weights are related to the prior information of the signal $\boldsymbol{\gamma}$, which can not be constructed precisely without first knowing $\boldsymbol{\gamma}$. Therefore, an iterative algorithm is used to estimating $\boldsymbol{\gamma}$ and redefining the weights

$$\begin{cases} \hat{\boldsymbol{\gamma}}^{(k)} = \min \left\| \mathbf{W}^{(k)} \boldsymbol{\gamma} \right\|_1 \quad \text{s.t.} \quad \left\| \boldsymbol{\Phi}\boldsymbol{\Psi}\boldsymbol{\gamma} - \mathbf{y} \right\|_2 \leq \varepsilon \\ w_i^{(k+1)} = \frac{1}{\gamma_i^{(k)} + \delta}, \quad i = 1, 2, \ldots L \end{cases} \tag{24}$$

Without loss of generality, a preliminary imaging result obtained by Fourier transform is adopted to construct the initial weights. Although the imaging quality is limited by high silelobes, an approximate imaging profile can be extracted from the preliminary result. Then, the initial weights can be constructed by (23) and the final image can be obtained by (24).

4. SIMULATION RESULTS

In this section, to verify the validity of the proposed imaging algorithm for 4-D SAR, the imaging experiments are carried out with respect to simulated data.

The main parameters used for simulation are as follows: the radar carrier frequency is 1.3 GHz, the flight height and the centre of ground range are all 5000 m, the baseline length is 500 m, the maximum unambiguous imaging range of height is 40 m, and the maximum unambiguous imaging range of velocity is 0.288 m/year. Supposed that there are two targets located in the scene at $s_1 = -2$ m and $s_2 = 2$ m with a signal-to-noise ratio of 10 dB each, and that moved with mean velocities $v_1 = 0.02$ m/year and $v_2 = -0.05$ m/year, respectively.

Let us refer the system geometry depicted in Figure 1. Considering $M = 1$ pass over the interested area at a fixed time, and then repeating the above experiment at $N = 25$ different times. The investigated scene has a height extension of $2s_o = 20$ m and a velocity extension of

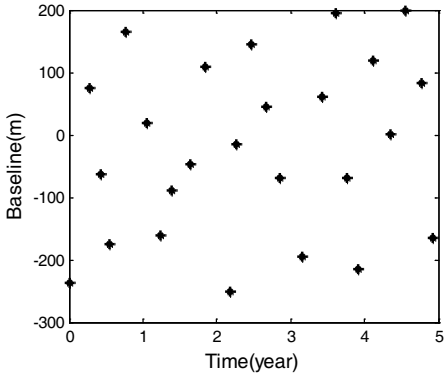

Figure 2. The position distributions of each pass in the baseline-time plane.

$2v_o = 0.2\,\mathrm{m/year}$. The non-uniform position distributions of each pass in the baseline-time plane are shown in Figure 2.

In order to analyze the performance of the proposed method, the imaging results obtained by the Fourier transform and the SVD methods are also given for comparison. Figure 3(a) shows the height-velocity reconstruction result obtained by the Fourier method. From Figure 2, we can get that the observation data received by the 4-D SAR system is sparse and non-uniform in the baseline-time plane. Therefore, the Fourier estimated height-velocity image is impaired by intolerable sidelobes. Figure 3(b) shows the height-velocity reconstruction result obtained by the SVD method. Since a prior knowledge of investigated scene is taken into account, a reduction of the sidelobes can be acquired by this method. A realization of the CS-based height-velocity reconstruction image is shown in Figure 3(c). As a favorable sparse reconstruction technique, CS reconstructs spectral lines instead of sinclike point response functions and shows a lower sidelobes interference, overcoming the imaging quality limitation imposed by the low number of flight tracks and their non-uniform distributions. And Figure 3(d) is the height-velocity reconstruction result obtained by the weighted CS method. From Figures 3(c) and (d), we can get that the imaging result can be improved after the weighted matrix introduced to the cost function.

The following case studies the influence of noise to the imaging algorithm. Maintaining the same parameters as above, the only difference is that the two targets with a signal-to-noise ratio of 0 dB each. Figure 4 shows the height-velocity reconstruction images with Fourier, SVD, CS, and weighted CS methods, respectively. From

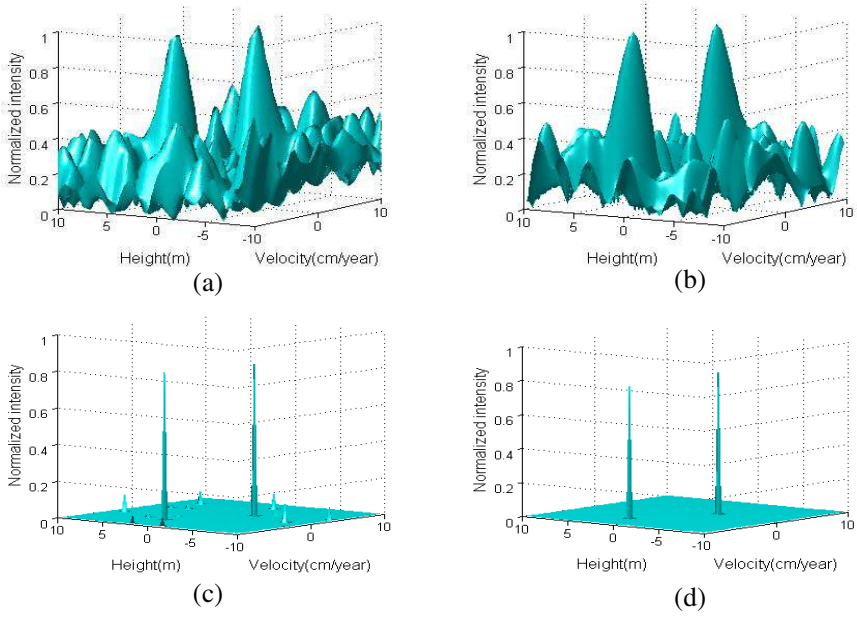

Figure 3. Comparison of the height-velocity imaging results of 4-D SAR with a signal-to-noise ratio of 10 dB. Shown are the results obtained by (a) fourier, (b) SVD, (c) CS, and (d) weighted CS.

Figure 4, the reconstruction images obtained by Fourier and SVD suffer from high sidelobes, and the image quality of CS is also influenced with lots of false targets under low noise level. However, the weighted CS method can reduce the sidelobes at

The coming to analysis takes into account four targets, with the different scattering factors, located at the same range and azimuth coordinates and with the height and velocity values equal to (2, 0.02), (2, -0.05), (-2, 0.02) and (-2, -0.05), respectively. The imaging results, obtained by the weighted CS method with different SNR levels, are represented in Figure 5. It can be observed that the lowest amplitude target located at (2, -0.05) is hidden by false targets under low noise level. However, for an SNR equal to 10 dB, the method based on weighted CS exhibits a close match to the truth: The targets are detected with accurate amplitudes at the right positions. The results presented in this case show that the imaging quality of weighted CS processing will become unsatisfactory when the difference of targets' scattering factor is large under low SNR level. Nevertheless, the imaging result will be acceptable with the increasing of the SNR.

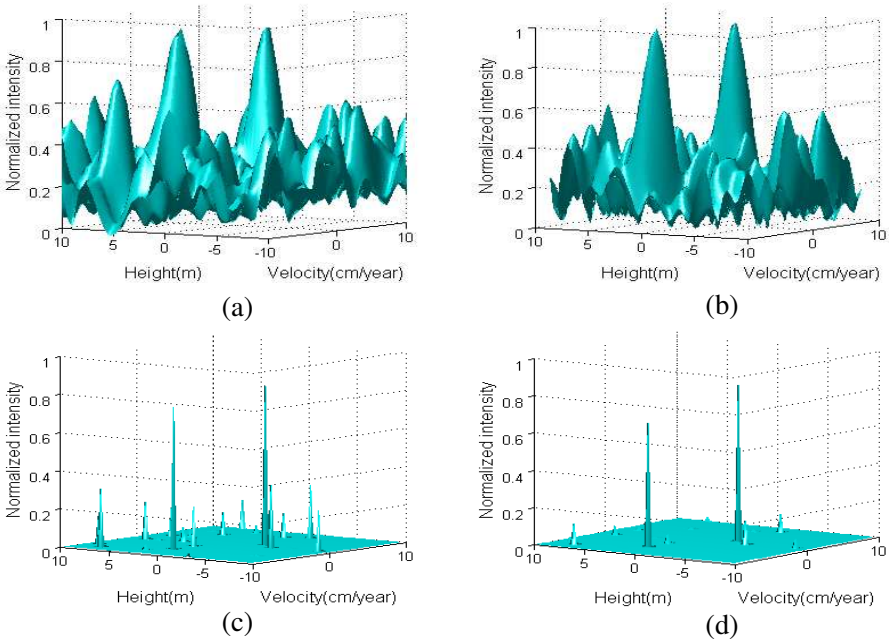

Figure 4. Comparison of the height-velocity imaging results of 4-D SAR with a signal-to-noise ratio of 0 dB. Shown are the results obtained by (a) Fourier, (b) SVD, (c) CS, and (d) weighted CS.

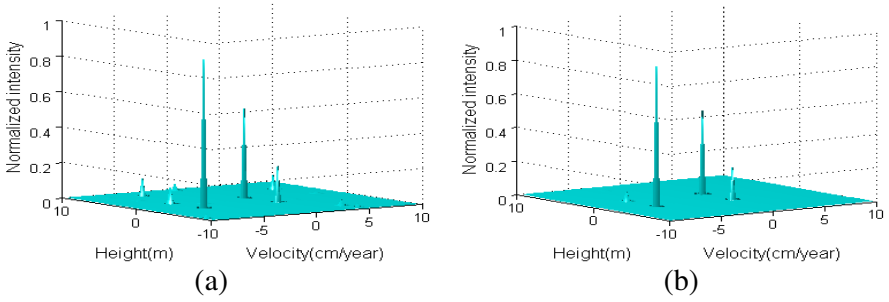

Figure 5. Imaging results obtained by the weighted CS method with different SNR levels. Shown are the results obtained with (a) SNR = 0 dB, (b) SNR = 10 dB.

5. CONCLUSION

4-D SAR imaging is an extension of the conventional microwave imaging technique. It extends the potentialities of SAR tomography to the target deformation monitoring, which enables not only separating interfering targets in height but also distinguishing their single slow deformation velocities. Therefore, 4-D SAR may have challenging potential for buried scatterers and subsurface dynamical processes investigations. In this paper, a novel 4-D SAR imaging method based on weighted compressive sensing has been proposed. The principle behind the method is based on considering the sparse structure of actual target space in high frequency radar application. The key step of this method is to construct the basis matrix and the measurement matrix using the sparse distribution of the radar positions and the signal form after the azimuth-slant range compression. Moreover, a weighted matrix is introduced into the optimization problem to reduce the influence of noise. The results of the simulated data confirm the effectiveness of the proposed method. Further work will focus on improving the cost function and evaluating the super resolution capability of this method.

ACKNOWLEDGMENT

This work was supported by the Key Laboratory of Ministry of Education, College of Information Science and Engineering, Henan University of Technology.

REFERENCES

1. Chan, Y. K. and V. C. Koo, "An introduction to synthetic aperture radar (SAR)," *Progress In Electromagnetics Research B*, Vol. 2, 27–60, 2008.
2. Tian, B., D. Y. Zhu, and Z. D. Zhu, "A novel moving target detection approach for dual-channel SAR system," *Progress In Electromagnetics Research*, Vol. 115, 191–206, 2011.
3. Chang, Y. L., C. Y. Chiang, and K. S. Chen, "SAR image simulation with application to target recognition," *Progress In Electromagnetics Research*, Vol. 119, 35–57, 2011.
4. Zhang, M., Y. W. Zhao, H. Chen, and W. Q. Jiang, "SAR image simulation for composite model of ship on dynamic ocean scene," *Progress In Electromagnetics Research*, Vol. 113, 395–412, 2011.

5. Reigber, A. and A. Moreira, "First demonstration of airborne SAR tomography using multibaseline L-band data," *IEEE Transactions on Geoscience and Remote Sensing*, Vol. 38, No. 5, 2142–2150, 2000.
6. Ren, X. Z., L. H. Qiao, and Y. Qin, "A three-dimensional imaging algorithm for tomography SAR based on improved interpolated array transform," *Progress In Electromagnetics Research*, Vol. 120, 181–193, 2011.
7. Regiber, A. and R. Scheiber, "Airborne differential SAR interferometry: First results at L-band," *IEEE Transactions on Geoscience and Remote Sensing*, Vol. 41, No. 6, 1516–1520, 2003.
8. Wu, B. I., M. C. Yeuing, Y. Hara, and J. A. Kong, "Insar height inversion by using 3-D phase projection with multiple baselines," *Progress In Electromagnetics Research*, Vol. 91, 173–193, 2009.
9. Lombardini, F., "Differential tomography: A new framework for SAR interferometry," *IEEE Transactions on Geoscience and Remote Sensing*, Vol. 43, No. 1, 1–8, 2005.
10. Soleimani, M., C. N. Mitchell, R. Banasiak, R. Wajman, and A. Adler, "Four-dimensional electrical capacitance tomography imaging using experimental data," *Progress In Electromagnetics Research*, Vol. 90, 171–186, 2009.
11. Goharian, M., M. Soleimani, and G. R. Moran, "A trust region subproblem for 3D electrical impedance tomography inverse problem using experimental data," *Progress In Electromagnetics Research*, Vol. 94, 19–32, 2009.
12. Wei, H. Y. and M. Soleimani, "Three-dimensional magnetic induction tomography imaging using a matrix free Krylov subspace inversion algorithm," *Progress In Electromagnetics Research*, Vol. 122, 29–45, 2012.
13. Banasiak, R., R. Wajman, D. Sankowski, and M. Soleimani, "Three-dimensional nonlinear inversion of electrical capacitance tomography data using a complete sensor model," *Progress In Electromagnetics Research*, Vol. 100, 219–234, 2010.
14. Serafino, F., F. Soldovieri, F. Lombardini, and G. Fornaro, "Singular value decomposition applied to 4D SAR imaging," *IEEE International Geoscience and Remote Sensing Symposium*, 2701–2704, Seoul, Korea, 2005.
15. Ren, X. Z. and R. L. Yang, "An inverse problem based approach for differential SAR tomography imaging," *Journal of Electronics & Information Technology*, Vol. 32, No. 3, 582–586, 2010.

16. Fornaro, G., F. Serafino, and D. Reale, "4D SAR imaging for height estimation and monitoring of single and double scatterers," *IEEE Transactions on Geoscience and Remote Sensing*, Vol. 47, No. 1, 224–237, 2009.
17. Wei, S. J., X. L. Zhang, J. Shi, and G. Xiang, "Sparse reconstruction for SAR imaging based on compressed sensing," *Progress In Electromagnetics Research*, Vol. 109, 63–81, 2010.
18. Wei, S. J., X. L. Zhang, and J. Shi, "Linear array SAR imaging via compressed sensing," *Progress In Electromagnetics Research*, Vol. 117, 299–319, 2011.
19. Budillon, A., A. Evangelista, and G. Schirinzi, "Three-dimensional SAR focusing from multipass signals using compressive sampling," *IEEE Transactions on Geoscience and Remote Sensing*, Vol. 49, No. 1, 488–499, 2010.
20. Zhu, X. X. and R. Bamler, "Tomography SAR Inversion by L_1-norm regularization — The compressive sensing approach," *IEEE Transactions on Geoscience and Remote Sensing*, Vol. 48, No. 10, 3839–3846, 2010.
21. Potter, L. C., P. Schniter, and J. Ziniel, "Sparse reconstruction for radar," *Proceedings of SPIE*, Vol. 6970, 697003-1–697003-15, Orlando, FL, USA, 2008.
22. Fornaro, G., F. Serafino, and F. Soldovieri, "Three-dimensional focusing with multipass SAR data," *IEEE Transactions on Geoscience and Remote Sensing*, Vol. 41, No. 3, 507–517, 2003.
23. Donoho, D. L., "Compressed sensing," *IEEE Transactions on Information Theory*, Vol. 52, No. 4, 1289–1306, 2006.
24. Candes, E. J., J. Romberg, and T. Tao, "Robust uncertainty principles: Exact signal reconstruction from highly incomplete frequency information," *IEEE Transactions on Information Theory*, Vol. 52, No. 2, 489–509, 2006.
25. Candes, E. J. and M. B. Wakin, "An introduction to compressive sampling," *IEEE Signal Processing Magazine*, 21–30, 2008.
26. Candes, E. J., M. B. Wakin, and S. P. Boyd, "Enhancing sparsity by reweighted l_1 minimization," *Journal of Fourier Analysis and Applications*, Vol. 14, No. 5, 877–905, 2008.